Atomistic simulation of AlO_x magnetic tunnel junction growth

Xiao Wang Zhou and Haydn N. G. Wadley

Department of Material Science and Engineering, University of Virginia, Charlottesville, Virginia 22904, USA

(Received 8 April 2004; revised manuscript received 23 September 2004; published 24 February 2005)

The tunneling magnetoresistance (TMR) of thin dielectric tunnel barriers that are sandwiched between pairs of ferromagnetic metal thin films is highly sensitive to the barrier layer atomic scale thickness, the uniformity in thickness, and the composition. Widely used AlO_x barriers are formed by the oxidation of 1–2 nm thick aluminum layers vapor deposited onto one of the ferromagnetic metal electrodes. The device is completed by vapor depositing the second ferromagnetic layer upon the oxide. Efforts to increase the TMR and tunneling conductance by reducing the thickness of the barrier have been successful until the aluminum layer thickness is decreased below ~1 nm whereupon the TMR disappears. The TMR loss is thought to occur because the oxide layer becomes discontinuous leading to regions of metal contact across the barrier layer in the completed device. Using a molecular dynamics simulation technique combined with a recently developed charge transfer potential for metal alloy oxides, we have investigated the atomistic scale phenomena responsible for the disruption of the oxide film's continuity. We show that discontinuous oxides always form during the oxidation of <0.6 nm thick crystalline aluminum films on (111) $Ni_{65}Co_{20}Fe_{15}$ single-crystal layers even when the precursor aluminum layer is continuous and of uniform thickness. The discontinuous mechanism of oxidation is shown to result from a surface-tension-driven dewetting as aluminum is converted to an amorphous oxide. The phenomenon establishes a lower limit of about 1 nm for the thickness of an aluminum oxide tunnel barrier fabricated by oxidation on (111) single-crystal $Ni_{65}Co_{20}Fe_{15}$ surfaces.

DOI: 10.1103/PhysRevB.71.054418 PACS number(s): 85.75.−d, 81.16.Pr, 85.70.Ay, 85.70.Kh

INTRODUCTION

The phenomenon of tunneling magnetoresistance (TMR) was first discovered by Julliere[1] in 1975 in Fe/Ge oxide/Co sandwich structures tested at very low temperatures. The magnetoresistance observed for this material system, however, was small. About ten years ago it was found that magnetic tunnel junctions (MTJ's) consisting of a pair of ferromagnetic metals separated by a thin (~1.5 nm) alumina dielectric tunnel barrier[2,3] exhibited a much larger tunneling magetoresistance ratio (~40–50 %) at ambient temperature.[4] These MTJ multilayers are beginning to be used for nonvolatile magnetic random access memory[2,5] and for magnetic field sensing.[6–8] Related tunneling barriers are also being evaluated for spin injection[9] in various spintronic devices.[10] Both a high tunneling conductance and TMR effect are desirable for all these applications.[2,6–8,11] First principles indicated that the conductance and TMR effect[12–15] are both sensitive to barrier layer thickness. They also indicate that the magnitude of the TMR effect depends sensitively upon the barrier height relative to that of the conduction band of the ferromagnetic layer. It also depends on the flatness of the barrier–ferromagnetic-metal interface and the perfection of bonding at the interface between the barrier and the ferromagnetic metal.

While numerous materials have also been studied, including AlN (Ref. 16) and MgO (Ref. 17), amorphous AlO_x is the most widely used barrier layer today.[2,3] Since it is difficult to achieve a uniformly thin dielectric layer by the direct deposition of the oxide, AlO_x layers are usually created by oxidizing a predeposited aluminum layer. Measurements of the magnetoresistance ratio (MR) of ferromagnetic metal/ AlO_x MTJ multilayers as a function of the aluminum layer thickness prior to oxidation[18,19] have revealed a rapid rise in MR as the barrier thickness is reduced (Fig. 1).[18] However, these measurements also reveal a surprising abrupt disappearance of the MR when the aluminum thickness is reduced below ~8 Å. It is thought that the formation of discontinuous AlO_x layers is likely to occur at a thin aluminum layer.[19,20] The subsequent deposition of the top ferromagnetic layer on an aluminum oxide layer containing holes would create regions of metal-to-metal contact and a high conductance path for electron transport that bypasses the tunneling barrier. To date, there have been no direct observations of the hole formation process published nor of the mechanisms by which such holes are formed.[21]

Molecular dynamics (MD) simulations of the vapor deposition are becoming an increasingly effective method for exploring the mechanisms of thin film growth during vapor

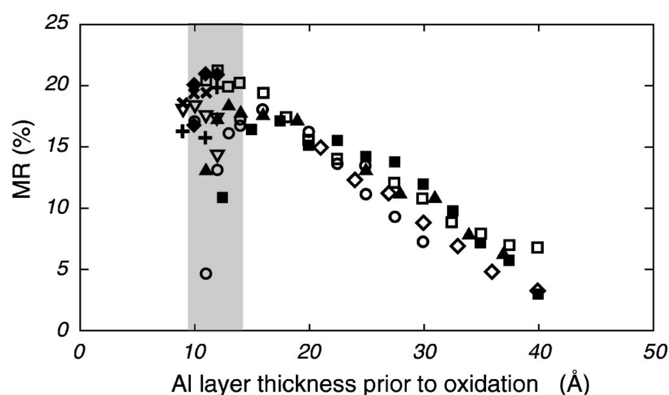

FIG. 1. Experimental MR ratio as a function of aluminum layer thickness prior to oxidation.[18] Different symbols refer to different oxidation times.

 ©2005 The American Physical Society

deposition and have begun to be used to study the growth of (metallic) giant magnetoresistive multilayers.[22–24] However, extensions of the approach to the reactive growth of an oxide layer must contend with the complexities of interatomic bonding in metal–metal oxide systems. Unlike all metallic systems where atom interactions can be well represented by relatively simple interatomic potentials such as the embedded atom method (EAM) potential,[25] atomic interactions in metal–metal oxide heterostructures are either predominantly ionic (in the oxide) or metallic (in the metal) depending on the local atomic surroundings. The character of the bonding therefore changes rapidly as one transverses through a metal/metal oxide interface.

A charge transfer ionic potential[26,27] (CTIP) has been used to address ionic interactions in heterostructures involving a single elemental metal and its oxide. By combining an EAM potential with a CTIP term, several groups have been able to use MD methods to simulate the oxidation of pure aluminum.[28,29] Extension of the simulations to the oxidation of metallic alloys has recently become feasible with the development of a modified CTIP that bounds the charge transfer by the valency of the atoms involved in oxidation.[30] Here, we use this modified CTIP together with an alloy EAM potential to simulate the formation of AlO_x barriers by oxidation of crystalline aluminum layers deposited on (111) single-crystal $Ni_{65}Co_{20}Fe_{15}$ ferromagnetic surfaces. The charge transfer between five elements O, Al, Ni, Co, and Fe were all dynamically treated during the reactive formation of the tunnel barrier.

MODELING METHODS

It is well established that the EAM potential describes well the interatomic forces between close-packed (fcc or hcp) metals such as Al, Co, Ni, and Fe.[22] For these metals, electrostatic interactions do not need to be explicitly considered because the charges on atoms in pure metal systems are negligibly small and the corresponding minor electrostatic effects have been implicitly included in the EAM parametrization. However, during the oxidation of these metals significant positive charges are induced on the metal atoms and significant negative charges are induced on the oxygen atoms. Additional complexity arises because the charges induced on these atoms are environment dependent. For instance, the charges on metal atoms change continuously from "zero" in a fully metallic region to a valency-determined maximum value in the stoichiometric oxide. The CTIP approach first proposed by Rappe and Goddard[26] and later by Streitz and Mintmire[27] allows the environment-dependent charges on the atoms to be dynamically deduced.

To simulate both metallic interactions and the additional variable electrostatic interactions due to atom ionization in metal/metal oxide heterostructures, an integrated potential combining both EAM and CTIP needs to be used.[27] For the integrated EAM+CTIP potential to be equivalent to the EAM potential of metals, the CTIP must predict zero charge and zero electrostatic interaction when used for pure metallic systems. Streitz and Mintmire's CTIP model has been combined with an EAM potential in this way,[27] and the resulting MD simulations of dynamic oxidation of pure aluminum provide detailed insights into the atomic mechanisms of oxidation.[28,29]

However, the original CTIP models[26,27] do not bound the charge transfer and this can lead to a violation of the classic concept of valency under some conditions. For instance, we find that when Streitz and Mintmire's CTIP model[27] is coupled with an EAM potential,[22,31] the simulations became divergent at small atomic separations because of nonphysical

TABLE I. EAM parameters for metals.

Metal	r_e(Å)	f_e	ρ_e	ρ_s	α	β	A (eV)
Al	2.86392	1.20378	17.51747	19.90041	6.61317	3.52702	0.31487
Ni	2.48875	2.21149	30.37003	30.37137	8.38345	4.47117	0.42905
Co	2.50598	2.31544	31.89166	31.89166	8.67963	4.62913	0.42138
Fe	2.48199	2.31453	24.59573	24.59573	9.81827	5.23641	0.39281
Metal	B (eV)	κ	λ	F_{n0} (eV)	F_{n1} (eV)	F_{n2} (eV)	F_{n3} (eV)
Al	0.36555	0.37985	0.75969	−2.80760	−0.30144	1.25856	−1.24760
Ni	0.63353	0.44360	0.82066	−2.69351	−0.07644	0.24144	−2.37563
Co	0.64011	0.50000	1.00000	−2.54180	−0.21942	0.73338	−1.58901
Fe	0.64624	0.17031	0.34061	−2.53499	−0.05960	0.19306	−2.28232
Metal	F_0 (eV)	F_1 (eV)	F_2 (eV)	F_3^- (eV)[a]	F_3^+ (eV)[a]	η (eV)	F_e (eV)
Al	−2.83	0.0	0.62225	−2.48824	−2.48824	0.78591	−2.82453
Ni	−2.70	0.0	0.26539	−0.15286	4.58568	1.01318	−2.70839
Co	−2.56	0.0	0.70585	−0.68714	3.09213	1.07702	−2.56584
Fe	−2.54	0.0	0.20027	−0.14877	6.69465	1.18290	−2.55187

[a]F_3^- and F_3^+ are used for $\rho \leq \rho_e$ and $\rho > \rho_e$, respectively.

TABLE II. EAM parameters for some pair potentials.

Pair	r_e(Å)	α	β	A (eV)	B (eV)	κ	λ
O-O	3.64857	5.44072	3.59746	0.34900	0.57438	0.08007	0.39310
O-Al	2.98520	8.49741	4.52114	0.09738	0.38121	0.18967	0.95234
O-Ni	2.95732	7.96528	4.42411	0.13521	0.25332	0.47077	0.65524
O-Co	2.59586	8.25224	4.37548	0.25714	0.34029	0.37419	0.50843
O-Fe	3.07992	7.52309	4.13330	0.17108	0.39869	0.22335	0.34380
Al-Ni	2.71579	8.00443	4.75970	0.44254	0.68349	0.63279	0.81777

increases in charge transfer.[30] In addition, these CTIP models only give zero charges for single-metal systems; they predict significant (nonphysical) charges on the atoms in a metal alloy system.[30] Because of this, they have only been used to study oxygen–single-metal (binary) systems.

Recently, we reported the development of a modified CTIP model that incorporates the principle of valency.[30] The modified CTIP can be combined with any EAM or other potential for stable simulations even at atomic spacings as small as 0.2 Å. In addition, this modified CTIP model predicts zero charge and zero electrostatic energy for any locally metallic (either elemental metal or metal alloy) region. In regions containing both oxygen and metals, it dynamically allows the ionization of oxygen and the metal atoms to create the anions and cations of the oxide and it accounts for their additional electrostatic energy contribution to the interatomic potential. This development now enables a direct MD simulation of the reactive growth of a MTJ multilayer.

To conduct simulations of MTJ layer oxidation, the modified CTIP has been combined with an alloy EAM potential to create a charge transfer potential for the O-Al-Ni-Co-Fe system. Details of the EAM+CTIP potential are described elsewhere,[30,32] and a complete set of parameters required to define all the potential functions for the O-Al-Ni-Co-Fe system is listed in Tables I–V. While most of the metal-metal pair potentials were constructed from the EAM alloy model,[22,31,33] the Al-Ni pair potential implemented here was fitted independently. The full integrated EAM and CTIP potential has been fitted to the lattice parameters, elastic constants, cohesive energies, vacancy formation energies, and crystal structures of the metals and metal oxides (corundum Al_2O_3, Fe_2O_3, and the $B1$ phases of CoO and NiO) of interest. The potential was then used with a Lagrangian implementation of a three-dimensional, thermostatically controlled molecular dynamics algorithm[22–24,34] to simulate the reactive synthesis of AlO_x tunnel barriers in a prototypical MTJ system.

RESULTS

An initial fcc $Ni_{65}Co_{20}Fe_{15}$ single-crystal substrate was made from 120 $(22\bar{4})$ planes in the x direction, 3 (111) planes in the y direction, and 16 $(2\bar{2}0)$ planes in the z direction [Fig. 2(a)]. It was created using the equilibrium (bulk) lattice parameter (a=3.604 Å) for fcc $Ni_{65}Co_{20}Fe_{15}$. Periodic boundary conditions were used in the x and z directions so that the crystal can be viewed as an infinitely large film lying on the x-z plane. A free boundary condition was used in the y direction so that vapor deposition could occur on the top y surface. The MD simulation approach was used first to deposit approximately six atomic layers of $Ni_{65}Co_{20}Fe_{15}$ on the initial (111) substrate surface. This was followed by the deposition of aluminum layers of various thickness. The vapor atoms were injected perpendicular to the growth surface, the substrate temperature was maintained at 300 K, and the deposition rate was 10 nm/ns as films were grown at various adatom energies between 0.1 and 5.0 eV.

An example of aluminum on $Ni_{65}Co_{20}Fe_{15}$ two-metal-layer crystal can be seen on the left of Fig. 2(a). It was obtained by depositing the $Ni_{65}Co_{20}Fe_{15}$ layer at a 4.0 eV adatom energy and the aluminum layer at a 0.2 eV adatom energy. We found that increasing the adatom energy resulted in much smoother $Ni_{65}Co_{20}Fe_{15}$ surfaces consistent with earlier findings in metal/metal multilayers.[22,24] We also discovered that relatively smooth aluminum surfaces were always obtained regardless of adatom energy. Further analysis indicated that this occurred because aluminum has a low Schwoebel barrier[35] facilitating the step flow mode of growth. In addition, aluminum has a relatively low cohesive energy (3.58 eV) compared to Ni (4.45 eV), Co (4.41 eV), and Fe (4.29 eV). As a result, the binding between aluminum and the underlying Ni, Co, and Fe atoms (with higher cohesive energies) is stronger than the binding between the aluminum atoms themselves. This also promotes wetting of aluminum on the $Ni_{65}Co_{20}Fe_{15}$ surface. However, epitaxial aluminum growth was complicated by the large lattice mismatch (~15%) between aluminum and $Ni_{65}Co_{20}Fe_{15}$. We found that misfit dislocations were formed in the bilayer system by mechanisms similar to those recently analyzed in detail in the (111) gold/permalloy system.[36,37]

The findings described above indicate that a relatively high adatom energy is required to grow a flat $Ni_{65}Co_{20}Fe_{15}$ surface but a low energy is acceptable for forming flat aluminum layers. The $Al/Ni_{65}Co_{20}Fe_{15}$ multilayers used for subsequent studies of oxidation were hence all grown using a high energy (4.0 eV) to deposit the $Ni_{65}Co_{20}Fe_{15}$ layer and a low energy (0.2 eV) to deposit the aluminum layer. The ef-

TABLE III. EAM parameters for oxygen electron density function.

f_e	Γ	Ψ
1.39478	2.11725	0.37457

TABLE IV. EAM parameters for oxygen embedding energy spline function.

i	$F_{0,i}$ (eV)	$F_{1,i}$ (eV)	$F_{2,i}$ (eV)	$F_{3,i}$ (eV)	$\rho_{e,i}$	$\rho_{\min,i}$	$\rho_{\max,i}$
0	−1.56489	−1.39123	1.77199	1.59833	54.62910	0	54.62910
1	−1.58967	1.30636	9.81033	0.00000	64.26953	54.62910	65.24078
2	−1.54116	2.02821	6.56240	0.00000	66.21202	65.24078	66.56797
3	−1.51798	2.30979	7.69582	0.00000	66.92391	66.56797	70.57748
4	−1.19082	4.12936	10.32338	0.00000	74.23105	70.57748	∞

fects of the aluminum layer thickness and uniformity upon the oxidation behavior were then both investigated.

Two crystals, one with about five atomic aluminum layers ($\sim$12 Å) and a second with only a single atomic aluminum layer ($\sim$2.5 Å), are shown on the left of Figs. 2(a) and 2(b). It can be seen that under the deposition conditions used, the aluminum layers in both samples have local thickness variations of around one atomic layer. It can also be seen that some aluminum atoms filled vacant sites in the $Ni_{65}Co_{20}Fe_{15}$ surface. This resulted in aluminum being dispersed (alloyed) in the top few planes of the $Ni_{65}Co_{20}Fe_{15}$ crystal.

Oxidation was initiated by introducing an atomic oxygen atmosphere above the $Al/Ni_{65}Co_{20}Fe_{15}$ multilayer. To ensure that a sufficiently thick oxide layer formed within the real time simulated ($\sim$1 ns), both a high oxygen vapor temperature (8000 K) and density (0.0003 oxygen atoms/Å^3) were used. The oxygen vapor density corresponded to a pressure of $\sim$12 atms of pure (atomic) oxygen. The experimental heat of the Al+O reaction[38] (which was used in the fitting of our potential) released about 8.4 eV per atomic oxygen atom that reacted with the aluminum crystal. The thermostatically temperature controlled molecular dynamics algorithm[34] conducted this thermal energy away from the surface and maintained a surface temperature close to 330 K during oxidation even though the heat of reaction and atomic oxygen collision rate with the solid surface were both very high.

The atomic configurations of two typical oxidized aluminum layers whose thickness prior to oxidation was about 12 and 2.5 Å are shown, respectively, on the right of Figs. 2(a) and 2(b). The formation of amorphous aluminum oxide layers was observed in all the simulations. This is consistent with experimental observations.[39] The composition of the AlO_x oxide layer increased from $x=0$ before oxidation to $x=1.55\pm0.05$ by the time oxidation ceased. The surface morphology of the AlO_x layers was found to be highly sensitive to the aluminum layer thickness prior to oxidation. It can be seen from Fig. 2(a) that the oxidation of the thicker aluminum layer resulted in the formation of a compositionally uniform, continuous, and flat AlO_x film. However, when the aluminum layer thickness was reduced to 2.5 Å [Fig. 2(b)], the AlO_x film was highly discontinuous and in some places much thicker than anticipated even though the aluminum layer prior to oxidation had been continuous and relatively smooth. Oxidation of the thin aluminum film resulted in the formation of holes in the AlO_x layer, exposing areas of the underlying $Ni_{65}Co_{20}Fe_{15}$ crystal.

The AlO_x oxide layer roughness could be quantified by taking the maximum difference in the layer thickness and dividing it by the average layer thickness. This relative roughness was calculated for many simulations and is shown in Fig. 3 as a function of the average aluminum layer thickness (prior to oxidation). When the aluminum layer thickness exceeded 6 Å, the AlO_x oxide layer roughness was relatively

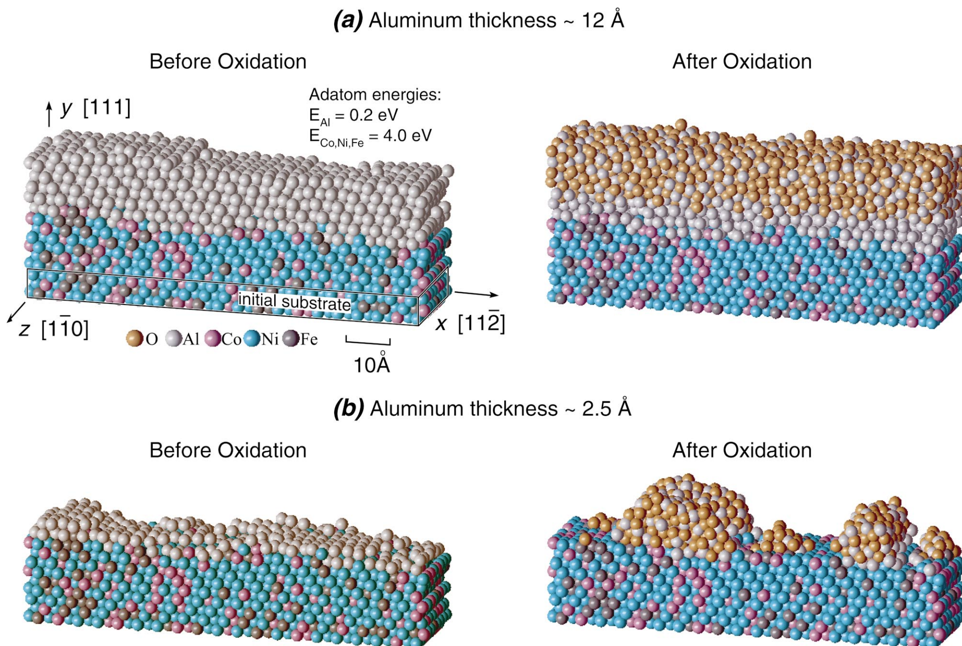

FIG. 2. (Color) Atomic configurations of (111) $Al/Ni_{65}Co_{20}Fe_{15}$ surfaces. (a) $\sim$12 Å aluminum layer thickness before oxidation (left) and after 60 ps exposure to 0.0003 oxygen atoms/Å^3 (right). (b) $\sim$2.5 Å aluminum layer thickness before oxidation (left) and after 100 ps exposure to 0.0003 oxygen atoms/Å^3 (right).

TABLE V. CTIP parameters for all elements.

Element	$q_{min}(e)$	$q_{max}(e)$	χ (eV)	J (eV)	$\xi(\AA^{-1})$	$Z(e)$
O	−2	0	2.00000	14.99523	2.144	0.00000
Al	0	3	−1.47914	9.07222	0.968	1.07514
Ni	0	2	−1.70804	9.10954	1.087	1.44450
Co	0	2	−1.67765	8.65773	1.055	1.54498
Fe	0	3	−1.90587	8.99819	1.024	1.28612

low. It can be seen that when the aluminum layer thickness was decreased below 6 Å, the AlO_x oxide layer roughness increased rapidly. This was found to correspond to the formation of holes. Further simulations using different random number seeds to initiate the runs indicated that at an aluminum layer thickness of between 6 and 10 Å, holes were formed with a probability that increased as the aluminum layer thickness was reduced. For all the simulations carried out at aluminum layer thicknesses above 10 Å, smooth oxide layers were obtained and no holes were observed. As a result, we conclude that for the crystal surfaces analyzed here, the critical aluminum layer thickness for smooth oxidation is around 10 Å. This finding appears to be consistent with the experimental observation of the loss of TMR when the preoxidation aluminum layer thickness was decreased below ~8 Å, (Fig. 1), and with other experimental studies.[16,19]

We also found that an increase of preoxidation surface roughness resulted in the formation of rough oxides at regions with thicker aluminum thicknesses. In these cases, holes preferentially formed at places where the aluminum layer thickness prior to oxidation was the thinnest.

The experimental thickness distribution of an aluminum oxide film synthesized by the oxidation of an aluminum layer on a ferromagnetic metal[40] is compared with that obtained from the MD simulations in Fig. 4. The oxide thickness distribution corresponding to the thicker simulated aluminum layer (average thickness $\bar{t}_{Al} \sim 6.4$ Å) was similar to that obtained in the experiments. However, the oxide thickness distribution for the thin aluminum layer ($\bar{t}_{Al} \sim 2.5$ Å) was much broader. The peak in the distribution occurred at a negative deviation of between 2.5 and 3.5 Å from the average oxide layer thickness ($\bar{t}_{AlO_x}$) of ~3.5 Å. This is consistent with a high fraction of the $Ni_{65}Co_{20}Fe_{15}$ surface not being covered by oxide.

To explore the role of the aluminum layer smoothness prior to the oxidation, the oxidation of "ideal" flat aluminum layers was investigated. Two (111) aluminum planes were first epitaxially added to a flat (111) $Ni_{65}Co_{20}Fe_{15}$ surface. This flat structure was found to be unstable because of the significant lattice mismatch between $Ni_{65}Co_{20}Fe_{15}$ and aluminum, and so the structure was stabilized by annealing at 900 K [Fig. 5(a)]. During annealing, many aluminum atoms migrated to form a partial third monolayer, leaving behind missing planes in the aluminum layer corresponding to misfit dislocations. The atoms in the third partial plane were subsequently removed [Fig. 5(b)], to create a uniformly thick, relatively perfect aluminum surface prior to oxidation. The crystal was then oxidized as described before, and the result is shown in Fig. 5(c). Once again, significant regions with no aluminum oxide coverage were observed.

DISCUSSION

To understand the driving force for hole formation, molecular statics calculations were used to determine the sur-

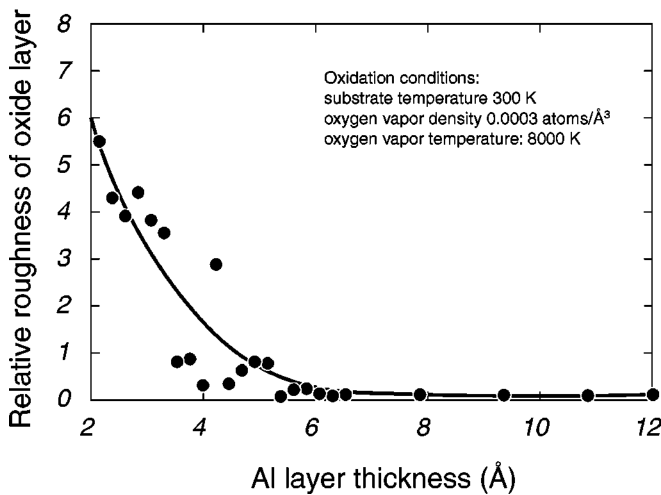

FIG. 3. Relative AlO_x layer roughness as a function of aluminum layer thickness prior to oxidation.

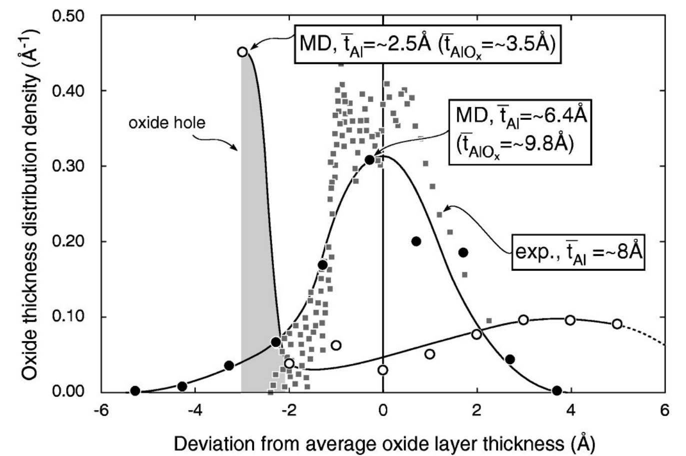

FIG. 4. Effects of aluminum layer thickness on the thickness distribution of the AlO_x layer. $\bar{t}_{Al}$ and $\bar{t}_{AlO_x}$ are average thicknesses of Al and AlO_x layers, MD and exp. refer to molecular dynamics simulations and experimental measurements, and oxide hole means zero oxide layer thickness.

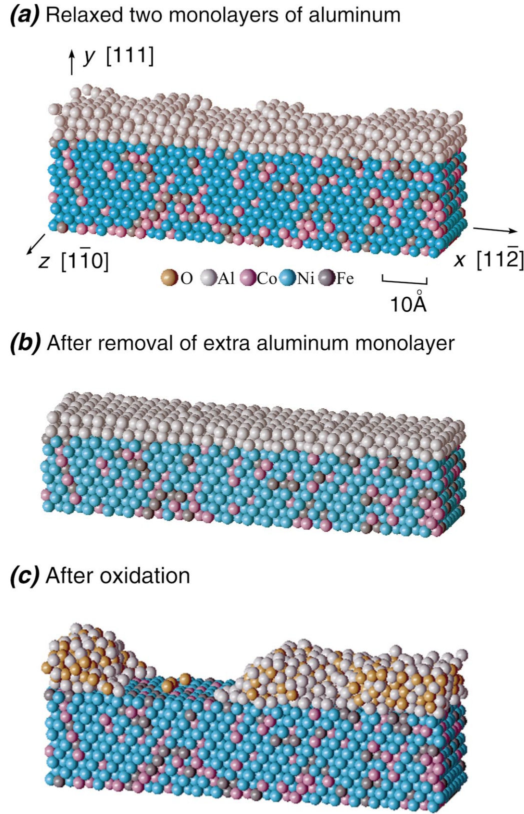

FIG. 5. (Color) Oxidation of an ideally flat (111) Al/$Ni_{65}Co_{20}Fe_{15}$ surface. (a) Thermally relaxed configuration from two epitaxial atomic aluminum layers on a flat (111) $Ni_{65}Co_{20}Fe_{15}$ surface. (b) Removal of the top (incomplete) atomic aluminum layer. (c) 90 ps after exposure to 0.0003 oxygen atoms/Å^3.

face and interface energies of the various phases. The surface energies of aluminum and $Ni_{65}Co_{20}Fe_{15}$ can be readily calculated from the total energy differences of bulk crystals and crystals bounded by two surfaces. The surface energy of an amorphous (bulk) Al_2O_3 phase can be similarly deduced once an amorphous structure is defined. This structure was created by first randomly disturbing the locations of atoms in an equilibrium Al_2O_3 corundum crystal and then annealing the structure using MD. Total energy calculations for a bulk sample and a sample with two surfaces then allow an estimate of the surface energy of this amorphous form of Al_2O_3.

To obtain interfacial energies, MD simulations were used to deposit Al on amorphous $AlO_{1.5}$, $Ni_{65}Co_{20}Fe_{15}$ on amorphous $AlO_{1.5}$, and Al on (111) $Ni_{65}Co_{20}Fe_{15}$. The resulting Al/$AlO_{1.5}$, $Ni_{65}Co_{20}Fe_{15}$/$AlO_{1.5}$, and Al/$Ni_{65}Co_{20}Fe_{15}$ interfaces were not ideally flat. Rather, they represented configurations similar to those encountered in the reactive MD simulations of MTJ deposition and incorporated many of the same defects (roughness, intermixing, vacancies, and misfit dislocations). These structures were then used to determine the interfacial energies at the three interfaces. The calculated surface energies σ and interfacial energies γ are summarized in Table VI.

Using Young's equation and the data from Table VI, the contact angle θ (see Fig. 6 for its definition) for aluminum on $Ni_{65}Co_{20}Fe_{15}$ can be evaluated from $\cos\theta=(\sigma_{NiCoFe}-\gamma_{Al/NiCoFe})/\sigma_{Al}\approx 1.72$. Since $\cos\theta$ is greater than 1, θ easily reaches zero, indicating that aluminum wets $Ni_{65}Co_{20}Fe_{15}$ well. It is also consistent with the observation reported above that flat aluminum layers can be readily grown on a $Ni_{65}Co_{20}Fe_{15}$ surface.

The contact angle for amorphous AlO_x on $Ni_{65}Co_{20}Fe_{15}$ can be calculated from $\cos\theta=(\sigma_{NiCoFe}-\gamma_{NiCoFe/AlO_x})/\sigma_{Al_2O_3}\approx -0.56$. This indicates a contact angle that is greater than 90°. As a result, amorphous AlO_x does not wet a (111) $Ni_{65}Co_{20}Fe_{15}$ single-crystal surface. Thus, we conclude that the formation of discontinuous AlO_x islands when thin aluminum layers are oxidized is a result of dewetting as the metallic aluminum is converted to amorphous AlO_x on the (111) $Ni_{65}Co_{20}Fe_{15}$ single-crystal surface.

The thermodynamic argument above identifies a driving force for the formation of discontinuous aluminum oxide layers. It is apparent that mass transport of both aluminum and oxygen must occur in order for discontinuous structures to be formed from initially uniform layers of aluminum. Estimates of the lateral transport distance can be made from an analysis of the in-plane positions of atoms. For the thicker aluminum layer shown in Fig. 2(a), oxidation resulted in an average lateral migration distance of about 2.4 Å for aluminum and of about 2.5 Å for oxygen in the 60 ps period of oxidation time. These migration distances are consistent with the short-range atomic reconstruction needed to form an amorphous structure. The corresponding migration distances on the thin aluminum layer [Fig. 2(b)] were about 8 Å for aluminum and 10 Å for oxygen.

During oxidation of thick aluminum layers, small AlO_x regions were nucleated continuously over the entire surface. During this process, oxygen vapor atoms were preferentially drawn to the least oxidized regions of the surface where they maximized the number of aluminum atoms they interacted with. This promoted the formation of a uniform oxide layer with a uniform Al:O ratio spatial distribution and was responsible for the short lateral diffusion distances.

Insights into the kinetic phenomena on a thin aluminum layer can be gained when a part of the surface is examined intermittently during its oxidation [Figs. 6(a)–6(f)]. Once a small region of the oxide had been nucleated [Fig. 6(c)], both nearby aluminum and oxygen atoms were laterally drawn into this oxide region. As oxidation continued, the lateral

TABLE VI. Surface energies of amorphous Al_2O_3, (111) Al, and (111) $Ni_{65}Co_{20}Fe_{15}$, and interfacial energies of (111)Al/amorphous AlO_x, (111) $Ni_{65}Co_{20}Fe_{15}$/amorphous AlO_x, and (111) Al/(111) $Ni_{65}Co_{20}Fe_{15}$.

Surface energy σ (eV/Å^2)			Interface energy γ (eV/Å^2)		
Al_2O_3	Al	NiCoFe	Al/AlO_x	NiCoFe/AlO_x	Al/NiCoFe
0.341	0.057	0.107	0.186	0.299	0.009

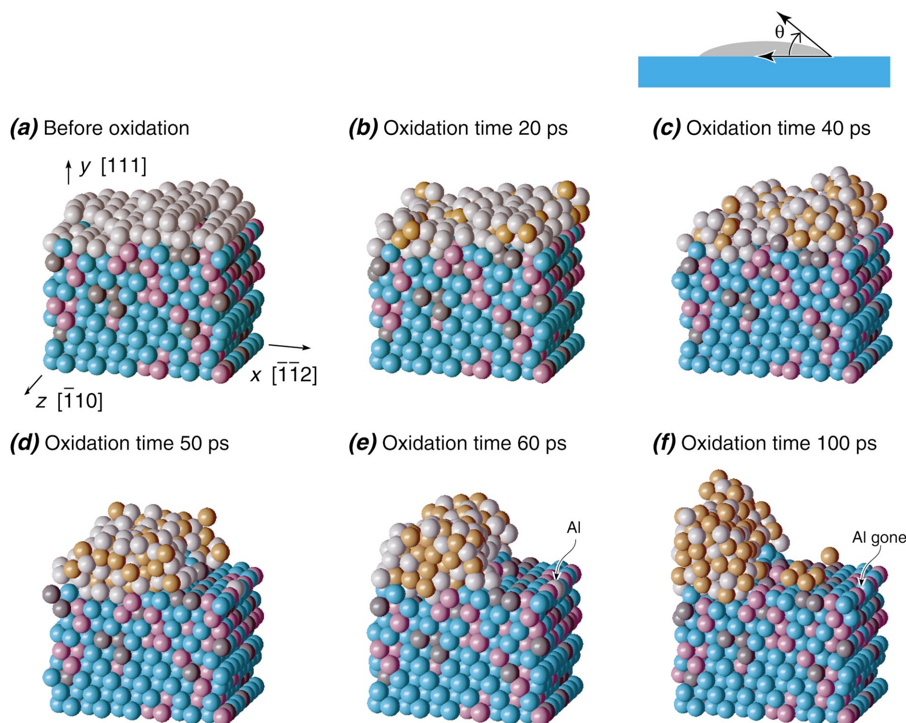

FIG. 6. (Color) Intermediate steps in the formation of a rough oxide film. (a) Before oxidation. (b) 10, (c) 20, (d) 30, (e) 40, and (f) 50 ps oxidation time.

migration of aluminum to the oxide depleted the aluminum coverage and the adjacent $Ni_{65}Co_{20}Fe_{15}$ surface became eventually exposed [Figs. 6(d)–6(f)]. Once this occurred, the oxide began to dewet and laterally shrink. This also resulted in a significant lateral migration of both the aluminum and oxygen atoms.

It is also interesting to note that aluminum atoms embedded in the $Ni_{65}Co_{20}Fe_{15}$ layer [Fig. 6(e)] are pulled out of the ferromagnetic layer during this oxidation. This and other observations indicate that oxidation dealloying of aluminum in the ferromagnetic layer can occur. It presumably improves the atomic (and electronic band) structure of the ferromagnetic layer at its interface with the oxide.

In micrometer thick oxide films, the oxidation is usually thought to exhibit parabolic kinetics.[41] For comparison, the oxidation of a ~15 Å aluminum layer on a $Ni_{65}Co_{20}Fe_{15}$ surface was used to investigate the early stages of oxidation. This aluminum layer is sufficiently thick to ensure the formation of a continuous AlO_x layer. The position of the Al/AlO_x interface, S, is shown in Fig. 7 as a function of oxidation time. It can be seen that the growth rate of the oxide was high when oxidation was first initiated. It then slowed with oxidation time. The data shown in Fig. 7 are not parabolic; they can be best fitted by $S=0.8358t^{0.3347}$ (S is in angstroms and t is in picoseconds). However, if we cast the data in pseudoparabolic form, the best fit then has the form $S=0.8358(k_\infty+t^{-0.1653})t^{1/2}$, where k_∞ is a small number that is negligible during the short simulated time but may dominate the kinetics after a prolonged oxidation is achieved. The parabolic rate coefficient is then time dependent and decreases to $0.8358k_\infty$ as time is increased.

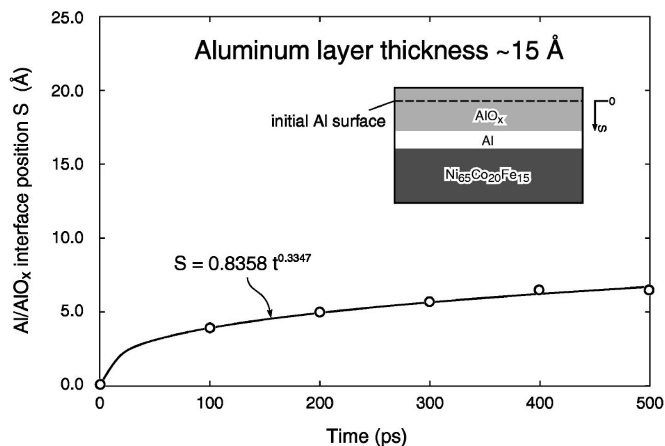

FIG. 7. Position of Al/AlO_x boundary as a function of oxidation time.

These results are consistent with the view that at the earliest stage of oxidation where the aluminum surface is fully exposed to oxygen atoms, the rate of reactive growth of the oxide layer is governed by the strong interaction between aluminum and oxygen atoms undergoing a barrierless (highly exothermic) reaction. Once a laterally complete oxide layer has formed on the surface, further thickening of the oxide layer requires diffusion through the oxide layer (surface oxygen toward the Al/AlO_x interface and bulk aluminum toward the surface). This results in an observed decrease in the parabolic rate constant that, if calculations had permitted, would approach that seen experimentally.

CONCLUSIONS

Molecular dynamics simulations performed using a modified charge transfer potential have identified the existence of a critical aluminum layer thickness below which discontinuous aluminum oxide layers are formed during the oxidation

of aluminum layers on a $Ni_{65}Co_{20}Fe_{15}$ surface. The critical thickness of the aluminum layer on a (111) $Ni_{65}Co_{20}Fe_{15}$ single crystal surface is determined by a dewetting phenomenon and lies between 0.6 and 1.0 nm when smooth, uniformly thick aluminum layers exist prior to oxidation. This minimum thickness is controlled by thermodynamic properties of the system. Further reductions in critical thickness might be achievable by modifying the ferromagnetic layer surface structure or adjusting its surface composition to reduce the contact angle of the amorphous aluminum oxide on its surface.

ACKNOWLEDGMENTS

This work was supported by Defense Advanced Research Projects Agency and Office of Naval Research through Grant No. N00014-03-C-0288. We are grateful to S. A. Wolf, S. S. P. Parkin, and D. X. Wang for helpful discussions of the work.

[1] M. Julliere, Phys. Lett. **54A**, 225 (1975).
[2] R. S. Beech, J. Anderson, J. Daughton, B. A. Everitt, and D. Wang, IEEE Trans. Magn. **32**, 4713 (1996).
[3] J. S. Moodera, L. R. Kinder, T. M. Wong, and R. Meservey, Phys. Rev. Lett. **74**, 3273 (1995).
[4] J. H. Yu, H. M. Lee, Y. Ando, and T. Miyazaki, Appl. Phys. Lett. **82**, 4735 (2003).
[5] M. Durlam, P. J. Naji, A. Omair, M. DeHerrera, J. Calder, J. M. Slaughter, B. N. Engel, N. D. Rizzo, G. Grynkewich, B. Butcher, C. Tracy, K. Smith, K. W. Kyler, J. J. Ren, J. A. Molla, W. A. Feil, R. G. Williams, and S. Tehrani, IEEE J. Solid-State Circuits **38**, 769 (2003).
[6] K. Shimazawa, J. J. Sun, N. Kasahara, K. Sato, T. Kagami, S. Saruki, O. Redon, Y. Fujita, T. Umehara, J. Syoji, S. Araki, and M. Matsuzaki, IEEE Trans. Magn. **37**, 1684 (2001).
[7] M. Tondra, J. M. Daughton, D. Wang, R. S. Beech, A. Fink, and J. A. Taylor, J. Appl. Phys. **83**, 6688 (1998).
[8] H. A. M. van den Berg, J. Altmann, L. Bar, G. Gieres, R. Kinder, R. Rupp, M. Vieth, and J. Wecker, IEEE Trans. Magn. **35**, 2892 (1999).
[9] V. F. Motsnyi, J. de Boeck, J. Das, W. Van Roy, G. Borghs, E. Goovaerts, and V. I. Safarov, Appl. Phys. Lett. **81**, 265 (2002).
[10] S. A. Wolf, D. D. Awschalom, R. A. Buhrman, J. M. Daughton, S. von Molnar, M. L. Roukes, A. Y. Chtchelkanova, and D. M. Treger, Science **294**, 1488 (2001).
[11] G. A. Prinz, Science **282**, 1660 (1998).
[12] W. H. Butler, X. G. Zhang, T. C. Schulthess, and J. M. MacLaren, Phys. Rev. B **63**, 054416 (2001).
[13] J. Mathon and A. Umerski, Phys. Rev. B **63**, 220403 (2001).
[14] J. M. MacLaren, X. G. Zhang, W. H. Butler, and X. Wang, Phys. Rev. B **59**, 5470 (1999).
[15] J. Mathon, Phys. Rev. B **56**, 11810 (1997).
[16] J. S. Moodera, L. R. Kinder, J. Nowak, P. LeClair, and R. Meservey, Appl. Phys. Lett. **69**, 708 (1996).
[17] J. S. Moodera and L. R. Kinder, J. Appl. Phys. **79**, 4724 (1996).
[18] W. Zhu, C. J. Hirschmugl, A. D. Laine, B. Sinkovic, and S. S. P. Parkin, Appl. Phys. Lett. **78**, 3103 (2001).
[19] J. S. Moodera, E. F. Gallagher, K. Robinson, and J. Nowak, Appl. Phys. Lett. **70**, 3050 (1997).
[20] J. H. Lee, H. D. Jeong, H. Kyung, C. S. Yoon, C. K. Kim, B. G. Park, and T. D. Lee, J. Appl. Phys. **91**, 217 (2002).
[21] D. J. Larson, A. K. Petford-Long, Y. O. Ma, E. W. Singleton, P. H. Clifton, B. W. Karr, and A. Cerezo (unpublished).
[22] X. W. Zhou, H. N. G. Wadley, R. A. Johnson, D. J. Larson, N. Tabat, A. Cerezo, A. K. Petford-Long, G. D. W. Smith, P. H. Clifton, R. L. Martens, and T. F. Kelly, Acta Mater. **49**, 4005 (2001).
[23] W. Zou, H. N. G. Wadley, X. W. Zhou, R. A. Johnson, and D. Brownell, Phys. Rev. B **64**, 174418 (2001).
[24] X. W. Zhou and H. N. G. Wadley, J. Appl. Phys. **84**, 2301 (1998).
[25] M. S. Daw and M. I. Baskes, Phys. Rev. B **29**, 6443 (1984).
[26] A. K. Rappe and W. A. Goddard, J. Phys. Chem. **95**, 3358 (1991).
[27] F. H. Streitz and J. W. Mintmire, Phys. Rev. B **50**, 11996 (1994).
[28] T. Campbell, R. K. Kalia, A. Nakano, P. Vashishta, S. Ogata, and S. Rodgers, Phys. Rev. Lett. **82**, 4866 (1999).
[29] S. Ogata and T. J. Campbell, J. Phys.: Condens. Matter **10**, 11449 (1998).
[30] X. W. Zhou, H. N. G. Wadley, J.-S. Filhol, and M. N. Neurock, Phys. Rev. B **69**, 035402 (2004).
[31] X. W. Zhou, R. A. Johnson, and H. N. G. Wadley, Phys. Rev. B **69**, 144113 (2004).
[32] X. W. Zhou and H. N. G. Wadley (unpublished).
[33] R. A. Johnson, Phys. Rev. B **39**, 12554 (1989).
[34] W. G. Hoover and B. L. Holian, Phys. Lett. A **211**, 253 (1996).
[35] M. Bockstedte, S. J. Liu, O. Pankratov, C. H. Woo, and H. Huang, Comput. Mater. Sci. **23**, 85 (2002).
[36] X. W. Zhou and H. N. G. Wadley, Philos. Mag. **84**, 193 (2004).
[37] F. M. Ross, K. M. Krishnan, N. Thangaraj, R. F. C. Farrow, R. F. Marks, A. Cebollada, S. S. P. Parkin, M. F. Toney, M. Huffman, C. A. Paz De Araujo, L. D. McMillan, J. Cuchiaro, M. C. Scott, C. Echer, F. Ponce, M. A. O'Keefe, and E. C. Nelson, MRS Bull. **21** (5), 17 (1996).
[38] *CRC Handbook of Chemistry and Physics* (CRC Press, Boca Raton, FL, 1978).
[39] L. F. Li, X. Y. Liu, and G. Xiao, J. Appl. Phys. **93**, 467 (2003).
[40] E. Z. Luo, S. K. Wong, A. B. Pakhomov, J. B. Xu, I. H. Wilson, and C. Y. Wong, J. Appl. Phys. **90**, 5202 (2001).
[41] A. J. Brock, G. R. Irani, and M. J. Pryor, Oxid. Met. **15**, 77 (1981).